Zirconium Transition Metal (Poly)antimonides – Syntheses, Characterization and Electrochemical Properties

Magnus Greiwe, Maximilian Krause, Oliver Osters, Alma Dorantes, Michele Piana, and Tom Nilges

Fachgebiet Synthese und Charakterisierung innovativer Materialien, Lehrstuhl für Technische Elektrochemie, Technische Universität München, Department Chemie, Lichtenbergstraße 4, 85747 Garching

Reprint requests to Prof. Dr. Tom Nilges. Fax: +49-(0)89-289-13762.
E-mail: tom.nilges@lrz.tum.de

Z. Naturforsch. **2013**, *68b*, 979 – 986 / DOI: 10.5560/ZNB.2013-3163
Received June 17, 2013

Herein we report on the syntheses, crystal structures and first electrochemical characterizations of ternary zirconium transition metal (poly)antimonides Zr_2TSb_3 (with T = Cu, Pd) and Zr_3TSb_7 (with T = Ni, Pd). The compounds were synthesized by arc-melting, followed by an annealing procedure at elevated temperatures. Phase analysis and structure analysis were performed by powder and single-crystal measurements. The electrochemical properties of all compounds were measured in half cells against lithium to test their potential as anode materials for Li batteries. The Zr_3TSb_7 phases show metallic behavior with conductivities of 10^{-1} S cm^{-1} within a temperature range of 324 to 428 K.

Key words: Polyantimonides, Zirconium, Transition Metals, Antimony

Introduction

The most common choices for anodes in lithium ion batteries are graphite or related carbon-based materials. Due to the low discharge specific capacity of 372 A h kg^{-1} and the necessity of 'Solid Electrolyte Interface' (SEI) formation during the first charge/discharge cycles in Li battery applications [1], an ongoing search for alternative materials is in progress. Group 15 elements and their compounds are one of the alternatives examined in this context. For instance, the high theoretical capacity of antimony against lithium (660 A h kg^{-1}) or of binary candidates like electrodeposited Sb/Sb_2O_3 nanocomposites (640 A h kg^{-1}) [2], drew the attention of the battery research community. There are many studies dealing with intermetallic compounds MSb_x (M = Ti, Mn, Fe, Co, Ni, Cu, Zn, In, Sn; x = 1 – 3) [3 – 5] showing discharge capacities in the order of graphite (330 A h kg^{-1} in the case of MSb with M = Ni, Co, Fe, Mn [3 – 5]), up to *ca.* 800 A h kg^{-1} for skutterudite-type $CoSb_3$ [6]. The performance of the latter compound, featuring covalently bonded antimony, led us to screen other polyantimonides for their potential usage as alternative anode materials. Another idea followed in the literature has been to use intermetallic compounds which show a similar structure in the lithiated and delithiated stage, like Cu_2Sb [7] or Fe_2Sb [8]. The reaction for Cu_2Sb against Li is reversible and delivers a steady capacity of 290 mA h g^{-1} after one conditioning cycle. For Fe_2Sb a capacity of 507 mA h g^{-1} was observed in the first cycle which cumulated in a reversible capacity of 282 mA h g^{-1} after 15 cycles.

Herein, we report on the characterization of ternary intermetallic Zr (poly)antimonides featuring a partially covalent character in the Sb network.

Results and Discussion

Crystal structures of Zr_3PdSb_7 and Zr_3NiSb_7

The crystal structures of Zr_3PdSb_7 and Zr_3NiSb_7 have been determined from single-crystal and powder data. All discussions in the text relate to single-crystal data of the Pd compound, unless otherwise stated. A section of the crystal structure is shown in Fig. 1 (left). The antimony atoms in Zr_3PdSb_7, with neighbors at distances between 3.120(1) and 3.179(1) Å, are forming a corrugated 4^4 net. The Sb–Sb distances are slightly longer than the bond lengths in α-antimony

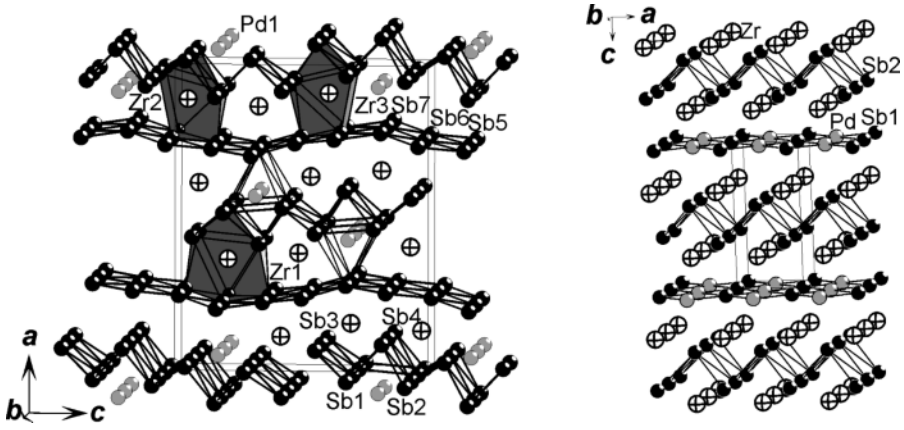

Fig. 1. Crystal structure sections of Zr_3PdSb_7 (left side) and Zr_2PdSb_3 (right side). Black lines are used to indicate the relationship between the two structures. Zr_3PdSb_7 is characterized by corrugated substructures, comparable with the planar arrangements in Zr_2PdSb_3.

(2.908 Å) within the layers, but shorter than the interatomic distance between the layers (3.355 Å) [9]. Bond lengths of 3.138 to 3.139 Å are reported for the 4^4 net in isostructural Zr_3NiSb_7 [10], in good accordance with the values of 3.136(1) and 3.137(1) Å observed by us. The shortest distance between Sb atoms in $ZrSb_2$ is 3.233 Å [11]. Hf_5Sb_9 as a candidate featuring a net with T-shaped, planar, covalent bonding at Sb atoms shows distances ranging from 2.989 to 3.026 Å [12]. For Hf_5Sb_9 a covalent character of the Sb–Sb bond has been discussed and substantiated by quantum-chemical calculations. Comparable Sb–Sb distances of 3.11 Å are found in $Zr_{11}Sb_{18}$ [13]. The only slightly larger Sb–Sb bond lengths in Zr_3PdSb_7 and Zr_3NiSb_7 (see also Table 1) are good indicators for covalent interactions in the Sb substructure.

Pd1 in Zr_3PdSb_7 is hexa-coordinated by Sb atoms forming a distorted $PdSb_6$ octahedron. Pd–Sb distances of 2.656(1) to 2.803(1) Å have been observed featuring the shortest distance to Sb7 of the 4^4 net. $PdSb_6$ octahedra share common edges to form an endless $[PdSb_2Sb_{4/2}]$ strand along the *b*axis. Two strands are connected to a double strand where each end of the double strand is terminated by Sb3. The distance between the octahedral and the terminal Sb3 is 3.644(1) Å. Zr is located between the 4^4 Sb net and the Pd/Sb double strands. Three crystallographically independent Zr positions are realized. The nearest neighbors are exclusively Sb atoms with distances of 2.963(1) to 3.189(1) Å, in good accordance with the range in related compounds like $Zr_{11}Sb_{18}$ (from 2.80 to 3.20 Å) [13]. This distance range is comparable to the longest ones in $ZrSb_2$ with bond lengths from 2.719 to 2.988 Å. Taking distances up to 3.2 Å (Fig. 1) into account, Zr2 and Zr3 are coordinated by Sb atoms forming a bi-capped trigonal prism while a tri-capped trigonal prism is realized for Zr1. The distance between the Zr atoms is 3.951(1) Å which is comparable with the distances in $ZrSb_2$ (Zr–Zr 3.987 Å) [11] and Zr_3NiSb_7 (Zr–Zr 3.927 Å) [10]. Zr_3NiSb_7 crystallizes isostructurally to the Pd compound. The specific distances in Zr_3NiSb_7 are shown in Table 1. They are found slightly shorter than in Zr_3PdSb_7 which correlates with the smaller atomic radius of Ni. The EDX analyses of the single crystals in at-% are Zr : Pd : Sb = 26(3) : 11(2) : 63(5) for Zr_3PdSb_7 and Zr : Ni : Sb = 25(4) : 12(3) : 63(7) for Zr_3NiSb_7, corresponding to the theoretical at-% ratio for both compounds of Zr : *T* : Sb = 27.3 : 9.1 : 63.6. The results of the refinement and the crystallographic data are shown in Tables 2, 3 and 4.

Table 1. Selected bond lengths (Å) of the Sb-Sb 4^4 net and the Pd/Ni-Sb_6 octahedra in Zr_3PdSb_7 and Zr_3NiSb_7 based on single-crystal data. Distances < 3.2 Å are presented. Standard deviations are given in parentheses.

Atoms	Zr_3PdSb_7	Zr_3NiSb_7
Sb5–Sb6	3.171(1)	3.137(1)
Sb5–Sb7	3.179(1)	3.136(1)
Sb6–Sb7	3.120(1)	3.140(1)
Pd1/Ni1–Sb1	2.704(1)	2.613(1)
Pd1/Ni1–Sb2	2.673(1)	2.584(1)
Pd1/Ni1–Sb4	2.803(1)	2.708(1)
Pd1/Ni1–Sb7	2.656(1)	2.576(1)

Electrical conductivity of Zr_3TSb_7 (T = Ni, Pd)

Phase-pure samples according to X-ray phase analyses have been used for the determination of the

Table 2. Crystallographic data and details of data collection of Zr_3TSb_7 (with T = Ni, Pd) derived from single crystals and powdered samples (Rietveld refinements). Standard deviations are given in parentheses.

Refined composition	Zr_3PdSb_7	Zr_3PdSb_7	Zr_3NiSb_7	Zr_3NiSb_7
Source of data	single crystal	Rietveld refinement	single crystal	Rietveld refinement
Crystal system	orthorhombic			
Space group	*Pnma* (no. 62)			
M_r, g mol^{-1}	1232.3		1184.6	
$D_{calcd.}$, g cm^{-3}	8.07	8.07	7.95	7.93
a, Å	17.6173(5)	17.6510(2)	17.5107(2)	17.5322(2)
b, Å	3.9450(2)	3.95110(3)	3.9239(8)	3.92841(4)
c, Å	14.5176(4)	14.5471(2)	14.3923(8)	14.4054(2)
V, Å^3	1008.98(6)	1014.53(2)	988.9(2)	992.15(2)
Z	4			
T, K	298(2)			
Radiation wavelength, Å	0.71073	1.5406	0.71073	1.5406
$F(000)$, e	2092		2020	
Refl. unique	1679	–	925	–
$\Delta\rho_{fin}$ (max / min), e Å^{-3}	4.89 / −4.62	3.76 / −4.33	3.15 / −3.09	4.45 / −5.90
Extinction coefficient	910(20)	–	280(20)	–
R_{int}	0.0505	–	0.0609	–
R_p	–	0.0599	–	0.0732
R_{wp}	–	0.0786	–	0.1002
$R(F)$ / $wR(F^2)$ (all refls.)	0.0317 / 0.0318	0.0977 / 0.0808	0.0269 / 0.0460	0.1048 / 0.1037
μ(MoK_α), cm^{-1}	23.4	–	24.0	–
μ(Cu$K_{\alpha1}$), cm^{-1}	–	187.1	–	178.7
GoF (F^2)	0.80	1.46	1.40	1.47

Table 3. Atomic coordinates and displacement parameters U_{iso} (Å^2) for Zr_3PdSb_7 derived from single-crystal data (plane) and from Rietveld refinement (*italics*). All atoms on Wyckoff position 4*c*. Standard deviations are given in parentheses; *y* coordinate in all cases 1/4.

Atom	x	z	U_{iso}
Sb1	0.01938(2)	0.30417(3)	0.00799(8)
	0.0200(3)	*0.3048(6)*	*0.040(3)*
Sb2	0.03623(2)	0.07158(3)	0.00772(8)
	0.0365(3)	*0.0714(5)*	*0.022(3)*
Sb3	0.07145(2)	0.56016(2)	0.00862(8)
	0.0716(3)	*0.5586(6)*	*0.047(4)*
Sb4	0.09290(2)	0.82411(2)	0.00818(9)
	0.0932(2)	*0.8171(6)*	*0.042(3)*
Sb5	0.22794(2)	0.35196(3)	0.00950(9)
	0.2284(3)	*0.3529(5)*	*0.031(3)*
Sb6	0.24834(2)	0.02008(2)	0.00882(8)
	0.2483(3)	*0.0211(5)*	*0.038(4)*
Sb7	0.28424(2)	0.68135(3)	0.01229(10)
	0.2825(3)	*0.6816(7)*	*0.056(3)*
Zr1	0.34753(3)	0.18933(4)	0.00793(12)
	0.3503(4)	*0.1873(7)*	*0.018(4)*
Zr2	0.36951(3)	0.46911(4)	0.00734(11)
	0.3686(5)	*0.4732(7)*	*0.031(4)*
Zr3	0.39227(3)	0.91170(4)	0.00783(12)
	0.3926(4)	*0.9114(6)*	*0.005(3)*
Pd1	0.43454(3)	0.69018(3)	0.00847(9)
	0.4354(4)	*0.6868(7)*	*0.035(3)*

Table 4. Atomic coordinates and displacement parameters U_{iso} (Å^2) for Zr_3NiSb_7 derived from single-crystal data (plane) and from Rietveld refinement (*italics*). All atoms on Wyckoff position 4*c*. Standard deviations are given in parentheses; *y* coordinate in all cases 1/4.

Atom	x	z	U_{iso}
Sb1	0.02144(3)	0.29775(4)	0.0106(2)
	0.0224(4)	*0.3020(7)*	*0.019(3)*
Sb2	0.03743(3)	0.07647(3)	0.0099(2)
	0.0384(4)	*0.0791(7)*	*0.025(4)*
Sb3	0.07109(3)	0.56064(4)	0.0110(2)
	0.0709(4)	*0.5622(5)*	*0.002(3)*
Sb4	0.09125(3)	0.82507(3)	0.0103(2)
	0.0917(3)	*0.8219(6)*	*0.002(3)*
Sb5	0.22819(3)	0.35399(4)	0.0112(2)
	0.2266(3)	*0.3523(5)*	*0.005(4)*
Sb6	0.24790(3)	0.02151(3)	0.0110(2)
	0.2496(4)	*0.0220(5)*	*0.008(3)*
Sb7	0.28996(3)	0.68546(4)	0.0147(2)
	0.2898(4)	*0.6896(7)*	*0.030(4)*
Zr1	0.34670(5)	0.19075(5)	0.0107(3)
	0.3496(5)	*0.1784(9)*	*0.017(5)*
Zr2	0.37049(5)	0.47074(5)	0.0098(2)
	0.3708(7)	*0.4739(12)*	*0.080(8)*
Zr3	0.39238(4)	0.91008(5)	0.0102(2)
	0.3915(5)	*0.9127(6)*	*–0.003(4)*
Ni1	0.43702(6)	0.68905(6)	0.0112(3)
	0.4403(8)	*0.6961(14)*	*–0.001(6)*

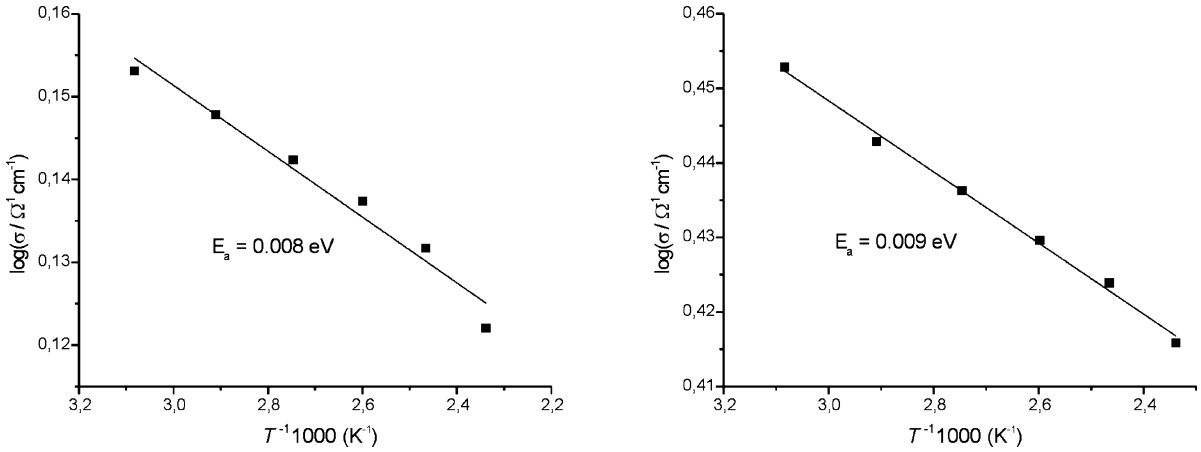

Fig. 2. Arrhenius plot of the total electrical conductivity of Zr_3NiSb_7 (left) and Zr_3PdSb_7 (right). Data are plotted for the temperature range 324 to 428 K.

electrochemical properties. The total electrical conductivity has been determined by impedance spectroscopy. In Fig. 2 an Arrhenius plot of the total electrical conductivity is shown. Obviously, the conductivity decreases with increasing temperature pointing towards a metallic character. At 324 K we derived total conductivities of 2.84 Ω^{-1} cm^{-1} for Zr_3PdSb_7 and 1.43 Ω^{-1} cm^{-1} for Zr_3NiSb_7. Conductivities in the order of 10^{-1} Ω^{-1} cm^{-1} indicate poor metallic behavior. These values are four orders of magnitude lower than the values for Zr_6NiSb_2 [14] and three orders of magnitude lower than for ZrNiSb [15]. In the Supporting Information (available online; see note at the end of the paper for availability) the total electrical conductivities of Zr_3TSb_7 (T = Ni, Pd) are stated.

Crystal structure of Zr_2PdSb_3 and Zr_2CuSb_3

Structures for Zr_2PdSb_3 (and Zr_2CuSb_3) have been derived from powder X-ray data after Rietveld refinements. Zr_2CuSb_3 has previously been similarly characterized [16], and the reported structure has now been used as a starting model for our structure determination. A summary of crystallographic data is given in Table 5, and structural details are highlighted in Table 6. A structure section of isotypic Zr_2TSb_3 (T = Cu, Pd) is shown in Fig. 1 (right). Sb1 is forming a planar 4^4 net, and Pd atoms occupy the centers of the squares. The Pd–Sb1 bond length is 2.811(1) Å in Zr_2PdSb_3, which is slightly larger than the distance between Sb and Pd in PdSb (2.737 Å) [17]. Sb2 forms a strongly corrugated 4^4 net in a zig-zag variation. The distance between neighboring Sb2 atoms is 3.466(2) Å. Zr atoms coordinating Sb2 in the first coordination sphere are forming a square pyramid. Each pyramid is sharing common edges with neighboring ones. The distance between the Pd and the Zr atoms is 3.048(2) Å which is longer than the distance of 3.022 Å between Zr and Cu in Zr_2CuSb_3 [16] and the distance in our Zr_2CuSb_3 sample of 3.040(1) Å. All relevant bond lengths are summarized in Table 7. In addition to the results of the Rietveld refinements we checked the ratio of the elements by EDX analyses. The results in at-% are Zr : Pd : Sb = 34(5) : 15(4) : 51(5) for the Zr_2PdSb_3

Table 5. Crystallographic data and details for Zr_2CuSb_3 and Zr_2PdSb_3, derived from Rietveld refinements. Standard deviations are given in parentheses.

Refined composition	Zr_2CuSb_3	Zr_2PdSb_3
Crystal system	tetragonal	
Space group	$P\bar{4}m2$ (no. 115)	
M_r, g mol^{-1}	611.2	654.1
$D_{calcd.}$, g cm^{-3}	7.46	7.90
a, Å	3.94967(8)	3.9749(2)
c, Å	8.7233(2)	8.7048(4)
V, Å^3	136.082(5)	137.54(1)
Z	1	
T, K	293	
Radiation wavelength, Å	1.5406	
$F(000)$, e	262	279
R_p	0.0595	0.0505
R_{wp}	0.0823	0.0645
$R(F)$ / $wR(F^2)$ (all refls.)	0.0646 / 0.0871	0.0610 / 0.0481
μ(Cu$K_{\alpha1}$), cm^{-1}	153.0	173.7
GoF (F^2)	1.84	1.07
$\Delta\rho_{fin}$ (max / min), e Å^{-3}	4.49 / −3.49	2.45 / −2.74

Table 6. Atomic coordinates and isotropic displacement parameters U_{iso} (Å^2) for Zr_2CuSb_3 and Zr_2PdSb_3 derived from Rietveld refinements. Standard deviations are given in parentheses.

Atom	Wyckoff positions	x	y	z	U_{iso}
Zr_2CuSb_3					
Sb1	1*a*	0	0	0	0.071(2)
Sb2	2*g*	0	1/2	0.6169(2)	0.0226(6)
Zr1	2*g*	0	1/2	0.2650(2)	0.024(2)
Cu1	1*b*	1/2	1/2	0	0.029(1)
Zr_2PdSb_3					
Sb1	1*a*	0	0	0	0.02(2)
Sb2	2*g*	0	1/2	0.6165(2)	0.0083(9)
Zr1	2*g*	0	1/2	0.2654(3)	0.013(1)
Pd1	1*b*	1/2	1/2	0	0.02(2)

Table 7. Selected bond lengths (Å) in Zr_2TSb_3 (T = Pd, Cu) based on powder data after Rietveld refinements. Standard deviations are given in parentheses.

Atoms	Zr_2PdSb_3	Zr_2CuSb_3
Sb1–Sb1	3.975(1)	3.950(1)
Sb1–Sb2	3.885(2)	3.882(1)
Sb2–Sb2	3.466(2)	3.458(1)
Sb2–Sb2	3.975(1)	3.950(1)
Sb1–Cu/Pd	2.811(1)	2.793(1)
Sb2–Cu/Pd	3.885(2)	3.882(1)
Sb2–Zr	2.993(1)	2.977(1)
Sb1–Zr	3.056(3)	3.040(1)
Cu/Pd–Zr	3.048(2)	3.040(1)

sample and Zr : Cu : Sb = 39(6) : 16(6) : 45(8) for the Zr_2CuSb_3 sample. In both batches we have not found particles with another ratio. The theoretical at-% ratio for both compounds is Zr : T : Sb = 33.3 : 16.7 : 50.0.

From a topological point of view the two structures show similarities in the Sb substructure. In both cases 4^4 net-like arrangements of Sb are realized, only varying in the grade of corrugation from M_2TSb_3 to M_3TSb_7. In M_2TSb_3, a planar 4^4 Sb/Pd net is neighbored by a corrugated Sb net, as shown in Fig. 1. By contrast, in the case of M_3TSb_7 the corrugated 4^4 net is fragmented into blocks which extend along the *b* axis. The planar 4^4 Sb/Pd net in M_2TSb_3 is slightly corrugated in M_3TSb_7, consisting of Sb atoms only in this case.

Electrochemical characterization

Reports in the literature state that most antimony compounds react with lithium to form Li_3Sb after a few cycles, with decreasing capacity in almost all cases. We are interested in antimony structures which show covalently bonded networks or substructures and want to test them as potential anode materials for Li batteries. Zr_2CuSb_3 and Zr_3NiSb_7, containing electrochemically active transition metals, show a more complex behavior upon cycling than the Pd-containing compounds.

Zr_2CuSb_3, as demonstrated in Fig. 3 (top left) shows several peaks for the lithiation and delithiation process. This phase thus exhibits many different electrochemical features, many more than all other tested candidates. In the first cycle a very complex behavior was observed (not shown in Fig. 3) pointing towards an irreversible capacity due to a high reactivity in the first cathodic sweep of the potential in the presence of Li^+ ions. Consecutive cycles up to the 20th show a small reduction peak at ~0.6 V_{Li} and a longer one at 0.8 V_{Li}. The potentials at which these peaks occur are in good agreement with the alloying reaction of Cu_2Sb with Li *via* Li_2CuSb to the final product Li_3Sb [18, 19]. An *ex-situ* examination of lithiated and delithiated cells is currently underway to substantiate this assumption.

Zr_3NiSb_7 (Fig. 3, bottom left) shows three peaks at 0.55, 0.75 and 0.8 V_{Li} in the second lithiation step of which the two former can not be observed after the fifth cycle. The 0.75 V_{Li} peak remains present upon further cycling for the next 50 cycles and slightly decreases up to the 90th cycle. Due to the fact that binary phases like NiSb and Ni_3Sb show peculiar electrochemical features [20] with potential plateaus in the same region as the peaks observed for Zr_3NiSb_7 (in the first five cycles), this strongly indicates the decomposition of the starting compound to the binary, electrochemically active species and their reversible reaction with Li afterwards. A detailed phase analysis of the half cells after the electrochemical test will substantiate this assumption.

The Pd phases are characterized by less distinct electrochemical features than the Cu or Ni counterparts. Zr_2PdSb_3 and Zr_3PdSb_7 (two graphs on the right hand side in Fig. 3) show reversible cycling with stable capacities up to 20 cycles, slightly decreasing for Zr_3TMSb_7 (TM = Ni, Pd) and more drastically for Zr_2PdSb_3 up to the 50th cycle.

All samples under discussion display a broad peak at 0.75 V_{Li} while charging. This peak is consistent with the reaction of Li and Sb to Li_3Sb according to $Sb + 3\,Li \rightarrow Li_3Sb$ [21].

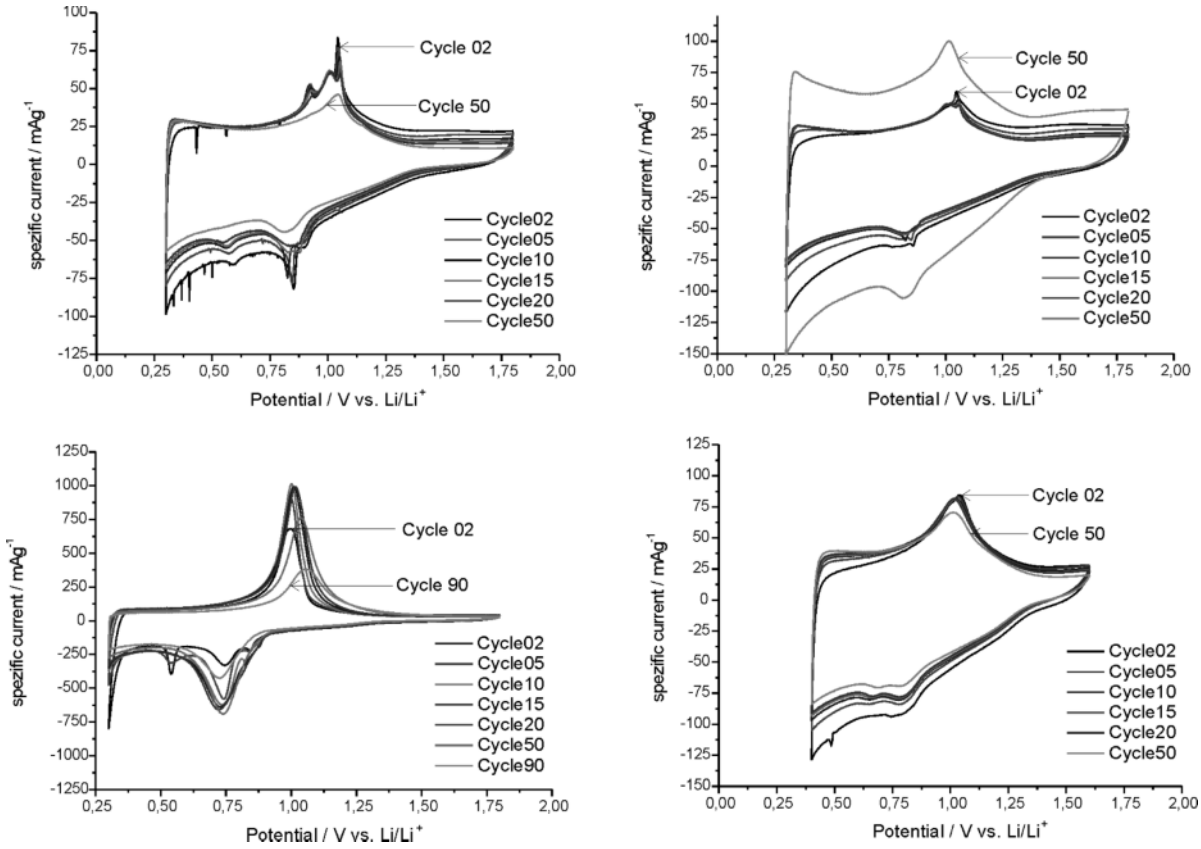

Fig. 3. CV data of Zr_2CuSb_3 (top left), Zr_2PdSb_3 (top right), Zr_3NiSb_7 (bottom left), and Zr_3PdSb_7 (bottom right). Half cells were fabricated according to the procedure given in the Experimental Section.

In none of the compounds presented here a reversible reaction of a ternary phase has been observed. It appears that decomposition takes place in the first cycles and reversibility is only due to binary T antimonides or elemental Sb. The role of Zr remains unclear and has to be examined in further experiments.

Conclusion

We have reported on the synthesis and characterization of Zr transition metal (poly)antimonides. Beside the structure redetermination of Zr_2CuSb_3 and Zr_3NiSb_7 and the electrochemical characterization of the latter, we succeeded in the synthesis and characterization of the two new representatives Zr_2PdSb_3 and Zr_3PdSb_7 in the ternary system Zr-Pd-Sb. Both compounds are isostructural to the known phases Zr_2CuSb_3 and Zr_3NiSb_7, respectively. Compounds Zr_3TSb_7 (T = Ni, Pd) are intermetallic phases showing conductivities of 1.43 and 2.84 Ω^{-1} cm^{-1} at 324 K, respectively. Electrochemical measurements in half cells against Li metal proved the occurrence of reversibility after the decomposition of the title compounds into binary phases. Unfortunately, the observed electrochemical performances are not sufficient to challenge present anode materials in battery applications.

Experimental Section

Syntheses of Zr_3TSb_7

0.5 g of Zr_3PdSb_7 and Zr_3NiSb_7 were synthesized by a home-made arc melting apparatus [22] under dry high-purity argon (purified over molecular sieves, silica gel and titanium sponge (1023 K)) on a water-cooled copper hearth. The starting materials were used without further purification in the form of granulates for Zr (99.8 %, ABCR), powder for Pd (99.9+ %, Chempur), wire for Ni (99+ %, Chempur) and

shots for Sb (99.999 %, Chempur). A ratio of Zr : (Pd, Ni) : Sb = 3 : 1 : 7 (in at-%) and a 10 wt-% excess of Sb were used for the syntheses. The Sb weight loss was between four and fourteen wt-% during the melting process in the arc furnace. The samples were melted three times, after each melting process step the regulus was turned around in order to yield a homogeneous sample. The metallic bulk regulus was finely ground afterwards, and the resulting powder was annealed at 973 K in evacuated quartz tubes for 7 d.

Syntheses of Zr_2TSb_3

0.5 g of Zr_2PdSb_3 and Zr_2CuSb_3 were synthesized in the same way as Zr_3TSb_7. A ratio of Zr : (Cu, Pd) : Sb = 5 : 1 : 9 (in at-%) and 4 wt-% excess of Sb were used for the syntheses.

Powder X-ray diffraction

Phase identification was carried out for powder samples using a STADIP X-ray diffractometer (Fa. Stoe, Darmstadt, Germany) using Cu$K_{\alpha 1}$ radiation ($\lambda = 1.54051$ Å and a germanium monochromator) with a Mythen 1K Detector (Fa. Dectris, Baden, Switzerland). An external calibration was performed with Si ($a = 5.43088$ Å). Data were collected from 5.015 to 115.010° 2θ. The XRD pattern was fitted using the Rietveld routine implemented in the program JANA 2006 [23]. The structure model derived from single-crystal data or from the literature was used as a starting model. For profile fitting we used a Pseudo-Voigt function, and a Legendre polynomial with 5 independent parameters for background description. All isotropic displacement parameters were refined without restrictions for each individual position. The cell parameters are $a = 17.6510(2)$, $b = 3.95110(3)$ and $c = 14.5471(2)$ Å and $V = 1014.53(2)$ Å^3 for the palladium and $a = 17.5322(2)$, $b = 3.92841(4)$ and $c = 14.4054(2)$ Å and $V = 992.15(2)$ Å^3 for the nickel compound. The cell parameters for Zr_2PdSb_3 are $a = 3.9748(2)$, $c = 8.7041(4)$ Å and $V = 137.52(1)$ Å^3 and for Zr_2CuSb_3 $a = 3.9496(1)$, $c = 8.7235(2)$ Å and $V = 136.08(1)$ Å^3. The Rietveld plots are shown in the Supporting Information.

Single-crystal X-ray diffraction

Single-crystal X-ray diffraction data collected on a Stoe IPDS II (Fa. Stoe, Darmstadt, Germany) fitted with a Mo tube ($\lambda = 0.71073$ Å) were used to determine the structures of Zr_3PdSb_7 and Zr_3NiSb_7. A numerical absorption correction [24] was performed independently for each data set based on an optimized crystal shape derived from the symmetry-equivalent reflections. The structure and crystallographic data are shown in Fig. 1 and Table 2. The compounds crystallize orthorhombically in space group *Pnma* (no. 62) with the lattice parameters $a = 17.6500(4)$, $b = 3.9509(1)$ and $c = 14.5460(3)$ Å and $V = 1014.34(4)$ Å^3 for the palladium and $a = 17.5107(2)$, $b = 3.9239(8)$ and $c = 14.3923(8)$ Å and $V = 988.9(2)$ Å^3 for the nickel compound.

Further details of the crystal structure investigations (single crystal and Rietveld data) may be obtained from Fachinformationszentrum Karlsruhe, 76344 Eggenstein-Leopoldshafen, Germany (fax: +49-7247-808-666; E-mail: crysdata@fiz-karlsruhe.de, http://www.fiz-informationsdienste.de/en/DB/icsd/depot_anforderung.html) on quoting the deposition number CSD-426312 (Zr_3NiSb_7), CSD-426314 (Zr_3PdSb_7), CSD-426313 (Zr_2CuSb_3, Rietveld data), and CSD-426315 (Zr_2PdSb_3, Rietveld data).

EDX analyses

Semi-quantitative EDX analyses were performed using a SEM 5900LV (JEOL, Tokyo, Japan) scanning electron microscope equipped with an INCA energy-dispersive microanalysis system (Oxford Instruments, Abingdon, Oxfordhire, UK). An acceleration voltage of 30 kV was used for the measurements. Another system we used was a desktop scanning microscope JCM-6000 NeoScop^{TM} (JEOL) equipped with an energy-dispersive X-Ray unit (JED-2200, Jeol). Here an acceleration voltage of 15 kV was applied for the measurements. In order to verify the compositions from structure analyses we measured exactly the crystals used for this experiment, in addition to four additional crystals separated from the same reaction batch.

Total electrical conductivity measurements

Pellets with 6 mm diameter of the powdered starting materials Zr_3PdSb_7 and Zr_3NiSb_7 were prepared by cold pressing (2 t applied pressure) of the respective powders. A density of 7.56 g cm^{-3} for the Pd and 7.21 g cm^{-3} for the Ni compound was achieved representing ~ 90 % of the theoretical density for Zr_3PdSb_7 and Zr_3NiSb_7, respectively. Each pellet was mounted between Pt electrodes and transferred to a home-made silica glass cell connected to a HP 4192A LF impedance analyzer (Agilent, Santa Clara, California, USA). A frequency range of 3 to 13 MHz was applied to the samples. The pellets were measured in the temperature range from 324 to 428 K.

Electrochemical measurements

The electrochemical behavior of the different antimony compounds against Li was determined, and their potential as an anode material for Li batteries was examined. Electrodes for half-cell measurements against Li metal were fabricated using a mixture of sample powders (85 wt-%) as active material, Super C65 (10 wt-%, TimCal) as a conductive additive and PVDF (Kynar HSV 900, 5 wt-%) as a binder. This mixture was homogeneously mixed with 1-methyl-2-

pyrrolidinone by stirring for 3 h at 333 K, then coated on a 0.1 mm thick copper foil using the Meyer rod technique with a wet film thickness of 80 μm. After drying the coating at 60 °C, 11 mm diameter electrodes were punched out of it and dried at 393 K in a Büchi oven to remove completely any solvent contamination. The final mass-loading of active material on the electrode was *ca.* 2 mg cm^{-2}. Electrochemical measurements were performed as counter and reference electrode in a polypropylene T-cell and a three-electrode setup using Li metal as both, counter and reference electrode. 1 M $LiPF_6$ in EC : DMC in a 1 : 1 w/w ratio was used as electrolyte (LP30, Merck). A Whatmann glass fiber filter separator Celgard 2325 was used, and the cell was completely filled with the electrolyte. Using a VMP3 potentiostat (Bio-Logic, Claix, France), cyclic voltammetry was carried out at room temperature at a scan rate of 0.5 mV s^{-1}, scanning the potential between 0.3 V_{Li} and 1.8 V_{Li} for all the samples except Zr_3NiSb_7, for which the range was between 0.4 V_{Li} and 1.6 V_{Li}, in order to avoid irreversible electrochemical reduction at potentials between 0 and 0.4 V_{Li}.

Supporting information

The full electrical conductivity data of Zr_3NiSb_7 and Zr_3PdSb_7 and the Rietveld plots of Zr_2CuSb_3, Zr_2PdSb_3, Zr_3NiSb_7 and Zr_3PdSb_7 are given as Supporting Information available online (DOI: 10.5560/ZNB.2013-3163).

Acknowledgement

This research was supported by the German Science Foundation (DFG) under Grant Ni 1095/4-1 as part of the PAK 77 program package. M. G. is grateful to the TUM Graduate School for support.

[1] C. Wang, A. J. Appleby, F. E. Little, *J. Electroanal. Chem.* **2001**, *497*, 33 – 46.
[2] H. Bryngelsson, J. Eskhult, L. Nyholm, M. Herranen, O. Alm, K. Edström, *Chem. Mater.* **2007**, *19*, 1170 – 1180.
[3] C. M. Ionica, P. E. Lippens, J. O. Fourcade, J.-C. Jumas, *J. Power Sources* **2005**, *146*, 478 – 481.
[4] J. Ren, X. He, W. Pu, C. Jiang, C. Wan, *Electrochim. Acta* **2006**, *4*, 1538 – 1541.
[5] V. Pralong, J. B. Leriche, B. Beaudoin, E. Naudin, M. Morcrette, J.-M. Tarascon, *Solid State Ionics* **2004**, *166*, 295 – 305.
[6] R. Alcántara, F. J. Fernández-Madrigal, P. Lavela, J. L. Tirado, J. C. Jumas, J. O. Fourcade, *J. Mater. Chem.* **1999**, *9*, 2517 – 2521.
[7] L. M. L. Fransson, J. T. Vaughey, R. Benedek, K. Edström, J. O. Thomas, M. M. Thackeray, *Electrochem. Commun.* **2001**, *3*, 317 – 323.
[8] J. Xie, X. B. Zhao, G. S. Cao, M. J. Zhao, Y. D. Zhong, L. Z. Deng, *Mater. Lett.* **2003**, *57*, 4673 – 4677.
[9] J. Donohue, *The Structures of the Elements*; Robert E. Krieger Publishing Co., Malabar, Florida, **1982**, p. 307.
[10] V. Romaka, A. Tkachuk, L. Romaka, *Acta Crystallogr.* **2008**, *E64*, i47.
[11] E. Garcia, J. D. Corbett, *J. Solid State Chem.* **1988**, *73*, 440 – 451.
[12] A. Assoud, K. M. Kleinke, N. Soheilnia, H. Kleinke, *Angew. Chem. Int. Ed.* **2004**, *43*, 5260 – 5262.
[13] I. Elder, C.-S. Lee, H. Kleinke, *Inorg. Chem.* **2002**, *41*, 538 – 545.
[14] G. Melnyk, E. Bauer, P. Rogl, R. Skolozdra, E. Seidl, *J. Alloys Compd.* **2000**, *296*, 235 – 242.
[15] H. Kleinke, *Z. Anorg. Allg. Chem.* **1998**, *624*, 1272 – 1278.
[16] N. Koblyuk, G. Melnyk, L. Romaka, O. I. Bodak, D. Fruchart, *J. Alloys Compd.* **2001**, *317 – 318*, 284 – 286.
[17] W. S. Kim, G. Y. Chao, *Can. Mineral.* **1991**, *29*, 401 – 409.
[18] M. Morcrette, D. Larcher, J.-M. Tarascon, K. Edström, J. T. Vaughey, M. M. Thackeray, *Electrochim. Acta* **2007**, *52*, 5339 – 5345.
[19] S. Tan, E. Perre, T. Gustafsson, D. Brandell, *Solid State Ionics* **2012**, *225*, 510 – 512.
[20] C. Villevieille, C. M. Ionica-Bousquet, A. De Benedetti, F. Morato, J. F. Pierson, P. Simon, L. Monconduit, *Solid State Ionics* **2011**, *192*, 298 – 303.
[21] M.-Z. Xue, Z.-W. Fu, *Electrochem. Commun.* **2006**, 1250 – 1256.
[22] R. Pöttgen, T. Gulden, A. Simon, *GIT Labor Fachz.* **1999**, *43*, 133 – 136.
[23] V. Petříček, M. Dušek, L. Palatinus, JANA2006 The Crystallographic Computing System; Institute of Physics, Praha (Czech Republic) **2006**.
[24] X-RED32, *Data Reduction Program* (version 1.53), X-SHAPE, *Crystal Optimization for Numerical Absorption Correction* (version 2.12.2), Stoe & Cie GmbH, Darmstadt (Germany), **2009**.